frontiers in Materials

ORIGINAL RESEARCH
published: 01 July 2021
doi: 10.3389/fmats.2021.703098

Structures, and Thermophysical Properties Characterizations of $(La_{1-x}Ho_x)_3NbO_7$ Solid Solutions as Thermal Barrier Coatings

*Lin Chen, Yitao Wang, Qi Zheng and Jing Feng**

Faculty of Material Science and Engineering, Kunming University of Science and Technology, Kunming, China

A sequence of $(La_{1-x}Ho_x)_3NbO_7$ solid solutions were fabricated in this work, which were studied as candidate for thermal insulation materials. The lattices were identified *via* XRD, when SEM and EDS were used to characterize the microstructures and element distributions. The results showed that the highest modulus, hardness, and toughness of $(La_{1-x}Ho_x)_3NbO_7$ were 196 GPa, 9.2 GPa, and 1.6 MPa $m^{1/2}$, respectively, and they accorded with the mechanical property requirements. Also, a low thermal conductivity (1.06 $W\,m^{-1}\,K^{-1}$) and high thermal expansion coefficients (TECs: 11.3 × $10^{-6}\,K^{-1}$) were simultaneously realized in $(La_{3/6}Ho_{3/6})_3NbO_7$, at high temperatures. No phase transition was detected up to 1,200°C, which proved their good high-temperature lattice stability. The intense anharmonic lattice vibrations might contribute to the outstanding thermal properties of $(La_{1-x}Ho_x)_3NbO_7$ ceramics. The suitable modulus, high hardness, low thermal conductivity, and high TECs of $(La_{1-x}Ho_x)_3NbO_7$ solid solutions proclaimed that they were exceptional thermal insulation ceramics.

Keywords: TBCs, oxides, structures, thermal conductivity, mechanical properties, niobates

OPEN ACCESS

Edited by:
Hao Zhang,
Jiangxi Science and Technology Normal University, China

Reviewed by:
Chunfeng Hu,
Southwest Jiaotong University, China
Xue Gong,
Shenyang Aerospace University, China
Weiwei Sang,
Henan University of Engineering, China

****Correspondence:***
Jing Feng
jingfeng@kust.edu.cn

Specialty section:
This article was submitted to Ceramics and Glass, a section of the journal Frontiers in Materials

Received: *30 April 2021*
Accepted: *07 June 2021*
Published: *01 July 2021*

Citation:
Chen L, Wang Y, Zheng Q and Feng J (2021) Structures, and Thermophysical Properties Characterizations of $(La_{1-x}Ho_x)_3NbO_7$ Solid Solutions as Thermal Barrier Coatings. Front. Mater. 8:703098. doi: 10.3389/fmats.2021.703098

INTRODUCTION

Diverse oxide ceramics are studied as candidate for thermal barrier coatings (TBCs), which are used to reduce the temperatures of superalloy parts (Padture et al., 2002; Clarke, 2003; Chen et al., 2011; Zhang et al., 2016; Zhang et al., 2017; Chen et al., 2018a; Liu et al., 2018; Chen et al., 2019a; Chen and Feng, 2019; Liu et al., 2019; Zhang et al., 2019; Zhou et al., 2019; Zhang et al., 2020; Zhou et al., 2020; Zhou et al., 2021). Good thermal insulations and a long service life are researched in TBCs, which require that oxides should possess low thermal conductivity, high thermal expansion coefficients (TECs), high hardness, and so on (Padture et al., 2002; Clarke, 2003; Yang et al., 2016; Zhang et al., 2016; Chen et al., 2018a; Zhou et al., 2019). Yttria-stabilized zirconia (YSZ) ceramics are widely researched and applied as TBCs, and they have good comprehensive thermophysical properties, including high hardness and fracture toughness, comparatively low thermal conductivity, and low density (Padture et al., 2002; Clarke, 2003; Chen et al., 2011). Since the phase transition of YSZ reduces its application temperature below 1,200°C, new materials are researched to replace it. $La_2Ce_2O_7$, $LnMgAl_{11}O_{19}$, $La_2Zr_2O_7$, and other oxides are extensively researched as TBCs to replace YSZ, and low thermal conductivity, high hardness, and good lattice stability are found in some oxides (Wang et al., 2012; Yang et al., 2016; Zhang et al., 2016; Zhang et al., 2017; Chen et al., 2019a; Liu et al., 2019). Among various ceramics, the ones with pyrochlore-/fluorite-type structures have lower thermal conductivity and better phase stability than YSZ. Hence, oxides having

pyrochlore-/fluorite-type structures are broadly studied, and thermophysical property improvements are essential for various materials (Ma et al., 2008; Wang et al., 2012; Wright et al., 2020; Adjaoud and Albe, 2021; Irum et al., 2021; Wang et al., 2021; Xiang et al., 2021; Zhang et al., 2021; Zhu et al., 2021).

The excellent thermophysical properties of pyrochlore-/fluorite-type $RE_2Zr_2O_7$ ceramics include low thermal conductivity (1–2 $W \cdot m^{-1} \cdot K^{-1}$, 25–1,000°C), high hardness (9–12 GPa), and good high-temperature phase stability (Wang et al., 2012; Yang et al., 2016; Liu et al., 2019; Wright et al., 2020; Xiang et al., 2021). One shortage of $RE_2Zr_2O_7$ is the inadequate fracture toughness (~1 MPa $m^{1/2}$), which stops it from being used as TBCs. Therefore, other oxides possessing pyrochlore-/fluorite-type structures are studied as TBCs. A_3BO_7-type rare earth niobates (RE_3NbO_7) have been studied in the past several years, and they have orthorhombic weberite and cubic fluorite lattices, which rely on RE^{3+} ionic size (Ma et al., 2008; Zhang et al., 2017; Yang et al., 2019; Chen et al., 2021a; Chen et al., 2021b; Xiang et al., 2021). The crystal structures of RE_3NbO_7 derive from fluorite A_4O_8, when the four A^{4+} ions are substituted by three RE^{3+} and one Nb^{5+} cation, and one oxygen vacancy is produced in the lattice to maintain charge balance (Wang et al., 2012; Chen et al., 2018a; Chen et al., 2021a; Chen et al., 2021b). RE_3NbO_7 is a weberite lattice when RE^{3+} ionic size is longer than 1.03 Å, and others are cubic fluorite with RE^{3+} size less than 1.03 Å. There are many similarities between crystal structures of RE_3NbO_7 and $RE_2Zr_2O_7$ ceramics. The lattices of RE_3NbO_7 and $RE_2Zr_2O_7$ originate from prototype fluorite A_4O_8; high concentration of oxygen vacancy (12.5%), [REO] polyhedrons, and excellent lattice stability are found in these two-type ceramics. Therefore, RE_3NbO_7 and $RE_2Zr_2O_7$ may have similar thermophysical properties.

Different structural and thermophysical property features are documented in weberite and fluorite RE_3NbO_7 oxides, and they display good thermal insulation performance (Chen et al., 2018b; Yang et al., 2019; Chen et al., 2021a; Chen et al., 2021b). The advantages of RE_3NbO_7 as TBCs include ultralow thermal conductivity, high TECs, and competitive modulus. The features of weberite and fluorite RE_3NbO_7 have been reported, and the differences of structures and properties between these two types of niobates are distinct. To study the variations of properties of RE_3NbO_7 along with the changes of lattice structures and to provide good understanding on these series niobates, the relevant study should be performed. The lowest thermal conductivity of weberite niobates is detected in La_3NbO_7, and the minimum thermal conductivity of fluorite niobates is found in Ho_3NbO_7 oxides (Chen et al., 2018b; Chen et al., 2019b; Yang et al., 2019; Chen et al., 2021a; Chen et al., 2021b). Dense $(La_{1-x}Ho_x)_3NbO_7$ solid solutions are fabricated in this work, and their lattices, thermal conductivity, hardness, and other properties are characterized. The variation trends of structures and thermophysical properties of $(La_{1-x}Ho_x)_3NbO_7$ are documented, which enables scholars to study their inner dominated mechanism from a good aspect.

EXPERIMENTS AND METHODS

The bulk samples of $(La_{1-x}Ho_x)_3NbO_7$ (x = 0/6, 1/6, 2/6, 3/6, 4/6, 5/6, and 6/6) solid solutions were fabricated *via* a high-temperature sintering process using La_2O_3, Ho_2O_3, and Nb_2O_5 powders (purity beyond 99.9% and a particle size smaller than 20 μm). The RE_2O_3 and Nb_2O_5 powders were weighted and then mixed in alcohol *via* a ball mill at a speed of 300r/min for 10 h, and then they were heated at 90°C for 6 h to remove alcohol. Approximately 1–2 g dry mixtures were taken and compressed *via* a tablet press under a condition of 300 MPa for 2 min. The green bodies of $(La_{1-x}Ho_x)_3NbO_7$ were finally sintered at 1,600–1700°C for 5–10 h to obtain their dense bulk samples. The lattice structures were identified *via* XRD (X-ray diffraction), and their surface microstructures were observed *via* a SEM (scanning electron microscope) and an EDS (energy dispersive spectrometer). The microhardness (H) and toughness (K_{IC}) were tested by an indentation test (DHV-1000Z-CCD, China), when Young's modulus (E) and mean acoustic velocity (V_a) were obtained by using an ultrasonic pulser/receiver equipment (UMS-100, France). The hardness and toughness of oxides were affected by bonding strengths, which were reflected *via* Young's modulus and Debye temperature (Θ_D) (Anderson, 1963; Schlichting et al., 2001):

$$\theta_D = \frac{h}{k_B}\left(\frac{3m}{4\pi V}\right)^{1/3} V_a, \tag{1}$$

where h, k_B, and m represented Plank's constant, the Boltzmann constant, and the lattice weight, respectively. As for thermal properties, TECs were measured *via* a TMA (thermal mechanical analysis), and thermal diffusivity (λ) was tested *via* a LFA to calculate thermal conductivity (k) (Schlichting et al., 2001):

$$k = \frac{\lambda \cdot \rho \cdot C_P}{1 - 4\phi/3}, \tag{2}$$

where ρ, C_P, and ϕ represented density, heat capacity, and porosity, respectively. Porosity was tested *via* an Archimedes balance, the weight (w_1) of sample was measured first, and then the sample was put in water to obtain its weight (w_2) under the action of water buoyancy; finally, the sample was taken out from water and wiped up to measure its weight (w_3). The porosity was calculated *via* a formula: $\phi = 1 - w_1/(w_3 - w_2)$. Thermal conductivity was calculated *via* phonons, and the corresponding phonon mean free path (l) was obtained *via* thermal diffusivity and average acoustic velocity (Kingery, 1955; Anderson, 1963; Kittle, 1996; Schlichting et al., 2001; Qu et al., 2012; Zhao et al., 2016; Wang et al., 2018; Ye et al., 2019):

$$l = 3\lambda / V_a, \tag{3}$$

where V_a was a constant, and it indicated that the temperature dependence of l relied on λ (Bruls et al., 2005). More details about sample preparations, structures identifications, and properties measurements could be found in our previous articles (Chen et al., 2018b; Chen et al., 2019b; Chen et al., 2021a).

RESULTS AND DISCUSSIONS

Structures Analysis

In the current work, the variations of properties along with the changes of lattices in $(La_{1-x}Ho_x)_3NbO_7$ oxides are studied. The

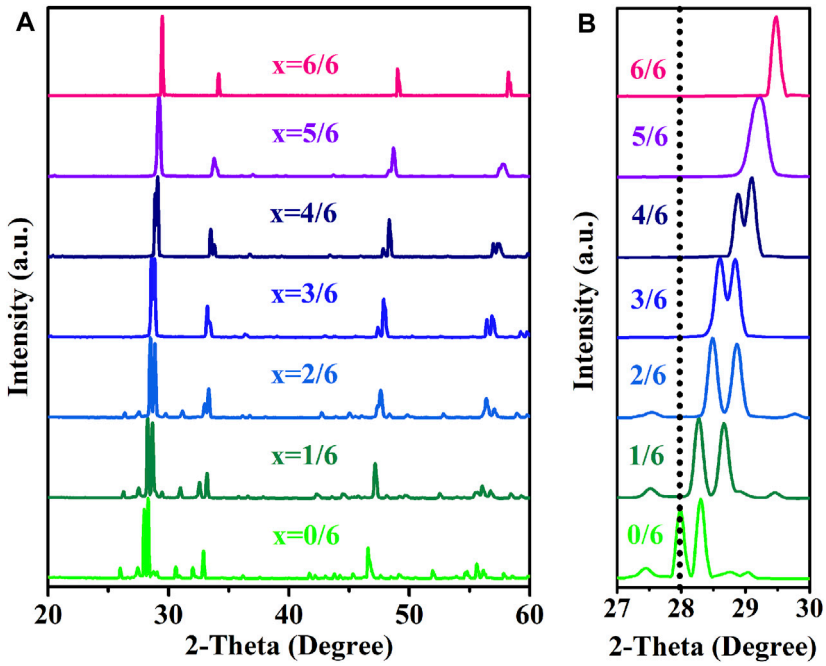

FIGURE 1 | The normalized XRD peaks of $(La_{1-x}Ho_x)_3NbO_7$ (x = 0/6, 1/6, 2/6, 3/6, 4/6, 5/6, and 6/6) ceramics: **(A)** 20°≤2-Theta≤60° and **(B)** 27°≤2-Theta≤30°.

TABLE 1 | The effective RE^{3+} size (rRE/Å), space group (SG), lattice constants (a, b, c/Å), unit cell volume (V/Å^3), theoretical density (ρ_0/g·cm^{-3}), and porosity (ϕ/%) of (La1-xHox)$_3$NbO$_7$ (x = 0/6, 1/6, 2/6, 3/6, 4/6, 5/6, and 6/6) ceramics.

x	r_{RE}	SG	a	b	c	V	ρ_0	ϕ
0/6	1.160	Cmcm	11.176	7.639	7.761	662.58	6.25	2.7
1/6	1.135	Cmcm	10.990	7.702	7.511	635.86	6.63	2.9
2/6	1.110	Cmcm	10.842	7.672	7.525	625.91	6.87	3.8
3/6	1.085	Cmcm	10.783	7.601	7.468	612.09	7.17	1.1
4/6	1.060	Cmcm	10.691	7.524	7.602	611.52	7.31	3.2
5/6	1.039	$C222_1$	10.612	7.535	7.477	597.88	7.63	3.7
6/6	1.015	$Fm\bar{3}m$	$a = b = c = 5.260$			145.53	7.98	2.2

normalized XRD peaks of prepared specimens are depicted in **Figure 1**, and it is found that three types of lattices are formed. When r_{RE} is 1.060–1.160 Å, the prepared samples (0/6 ≤ x ≤ 4/6) are in an orthorhombic phase with the space group (*SG*) of Cmcm; when r_{RE} is 1.039 Å, the prepared sample (x = 5/6) is in an orthorhombic phase with the *SG* of $C222_1$; and Ho_3NbO_7 is a cubic fluorite phase with $Fm\bar{3}m$ *SG*. The main XRD peaks shift to the right along with the decline of La content displayed in **Figure 1B**, which indicates the shrinkage of the lattice. **Table 1** exhibits the exact information of lattices of $(La_{1-x}Ho_x)_3NbO_7$ solid solutions. Some certain relationships can be constructed between cubic and orthorhombic $(La_{1-x}Ho_x)_3NbO_7$ lattice parameters. In cubic fluorite Ho_3NbO_7, it is found that $a_c = b_c = c_c$, when the lattice constants of orthorhombic $(La_{1-x}Ho_x)_3NbO_7$ are derived from the relationships of $a_o \approx 2a_c$, $b_o \approx 2^{0.5}b_c$, and $c_o \approx 2^{0.5}c_c$. The shrinkages of lattices and increments of unit cell mass lead to their theoretical density increases with the increasing Ho content. Also, **Table 1** exhibits that the porosity of each sample is 1–4%, and dense bulk samples are made in this work. The impacts of porosity on thermophysical properties are not taken into account.

The grain sizes of $(La_{1-x}Ho_x)_3NbO_7$ are a micron scale, and most grains have sizes of 1–20 μm shown in **Figure 2**. The good combinations among neighboring grains and a small grain size may result in good mechanical properties. The sintering temperatures of $(La_{1-x}Ho_x)_3NbO_7$ increase from 1,600 to 1700°C in conjunction with the increasing Ho content. Navrotsky's research showed that the formation enthalpy of RE_3NbO_7 became more exothermic with the increases of RE^{3+} ionic radius, which indicated that the sintering temperature decreased with the increasing RE^{3+} ionic size (Mielewczyk and Navrotsky, 2015; Chen et al., 2018b). Furthermore, the crystal structure is affected by RE^{3+} ionic radius, and fluorite RE_3NbO_7 has a smaller grain size than weberite RE_3NbO_7. Therefore, the grain size of $(La_{1-x}Ho_x)_3NbO_7$ is affected by the sintering temperatures and crystal structures, and they are dominated by RE^{3+} ionic radius. The increments of sintering temperature and order–disorder (weberite–fluorite) transition of crystal structure lead to a decrease of the grain size. **Figure 3** exhibits the backscattered electron (BSE) photo and the corresponding element mappings of $(La_{3/6}Ho_{3/6})_3NbO_7$. No precipitated phase is found, and each element is evenly distributed in this sample. The XRD, SEM, and EDS results prove that dense and high-purity $(La_{1-x}Ho_x)_3NbO_7$ samples are made via current methods.

Mechanical Properties

Equation 1 expresses that Debye temperature is proportional to the average acoustic velocity. **Figures 4A,B** exhibit that $(La_{1-x}Ho_x)_3NbO_7$ (0/6 ≤ x ≤ 2/6) oxides have similar Young's

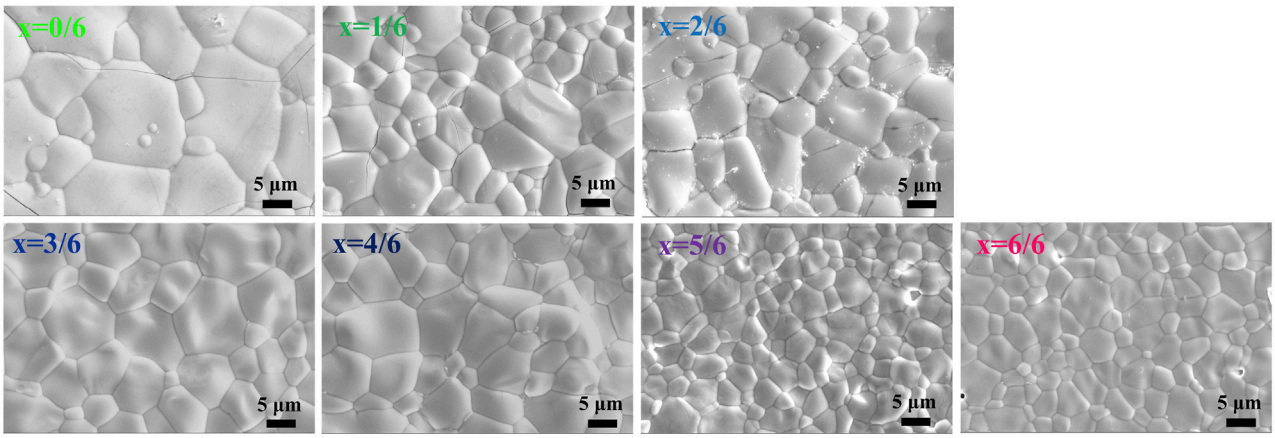

FIGURE 2 | Surface microstructure of $(La_{1-x}Ho_x)_3NbO_7$ (x = 0/6, 1/6, 2/6, 3/6, 4/6, 5/6, and 6/6) ceramics.

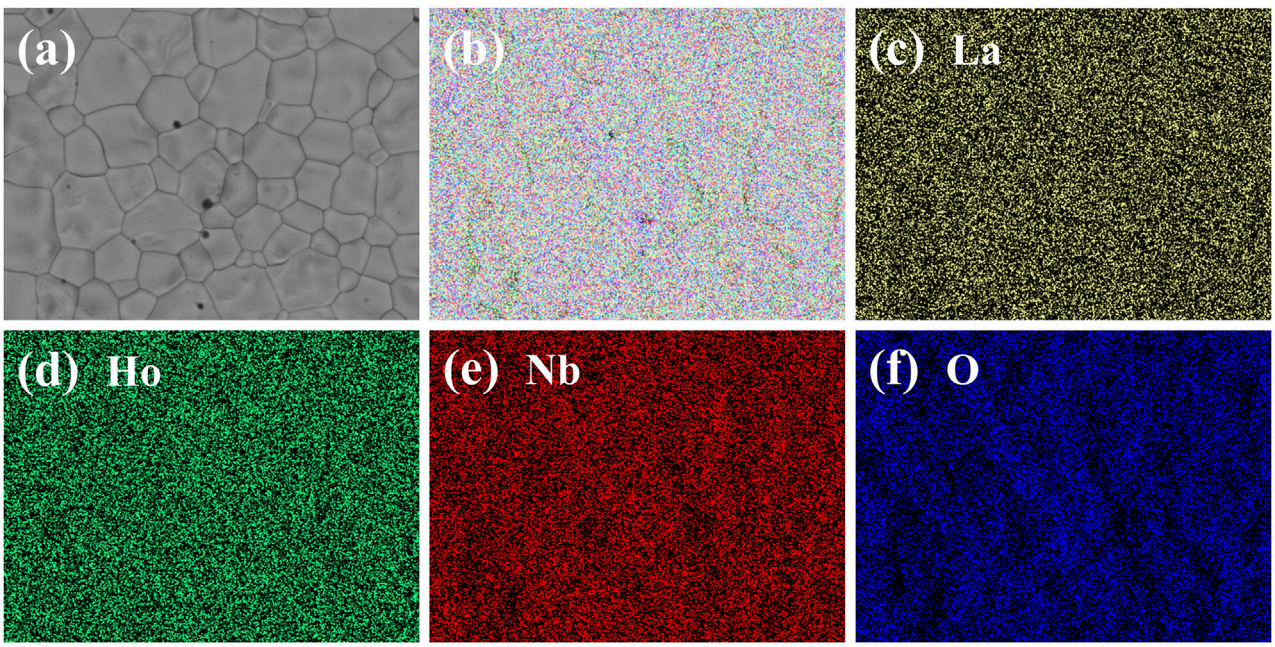

FIGURE 3 | SEM and EDS mapping photos of $(La_{3/6}Ho_{3/6})_3NbO_7$ ceramics: **(A)** BSE photo and **(B–F)** element mappings.

modulus (100–110 GPa) and Debye temperatures (310–340 K), implying that their bonding strengths are approximate. With the further increments of Ho content, $(La_{1-x}Ho_x)_3NbO_7$ ($3/6 \le x \le 6/6$) oxides have far higher Young's modulus (180–200 GPa) and Debye temperatures (390–420 K) than those of the aforementioned samples. Similar variation trends are found in hardness and toughness of the prepared samples, as shown in **Figures 4C,D**. $(La_{1-x}Ho_x)_3NbO_7$ ($3/6 \le x \le 6/6$) oxides have higher hardness and toughness than the remaining samples and their maximums are 9.2 ± 0.35 GPa and 1.6 ± 0.28 MPa $m^{1/2}$, respectively. The detail values of various mechanical properties are listed in **Table 2**. One can see that $(La_{1-x}Ho_x)_3NbO_7$ ceramics have higher hardness than $LaNbO_4$ (~3 GPa), while they have a lower value than YSZ (12–14 GPa), $RE_2Zr_2O_7$ (9–12 GPa), and $LaMgAl_{11}O_{19}$ (~14 GPa) (Wang et al., 2012; Chen et al., 2019a; Liu et al., 2019). Furthermore, $(La_{1-x}Ho_x)_3NbO_7$ ceramics have lower Young's modulus than YSZ (~250 GPa), $RE_2Zr_2O_7$ (240 GPa), and $LnMgAl_{11}O_{19}$ (300 GPa), while they have higher values than $LaNbO_4$ (60 GPa), Ho_2SiO_5 (150 GPa), and $REPO_4$ (140 GPa) (Vassen et al., 2000; Wang et al., 2012; Feng et al., 2013; Li et al., 2018; Chen et al., 2019a; Liu et al., 2019; Wu et al., 2020). The high modulus produces poor thermal stress fracture resistance, which is indicated by a so-called *TSR* parameter (Kingery, 1955):

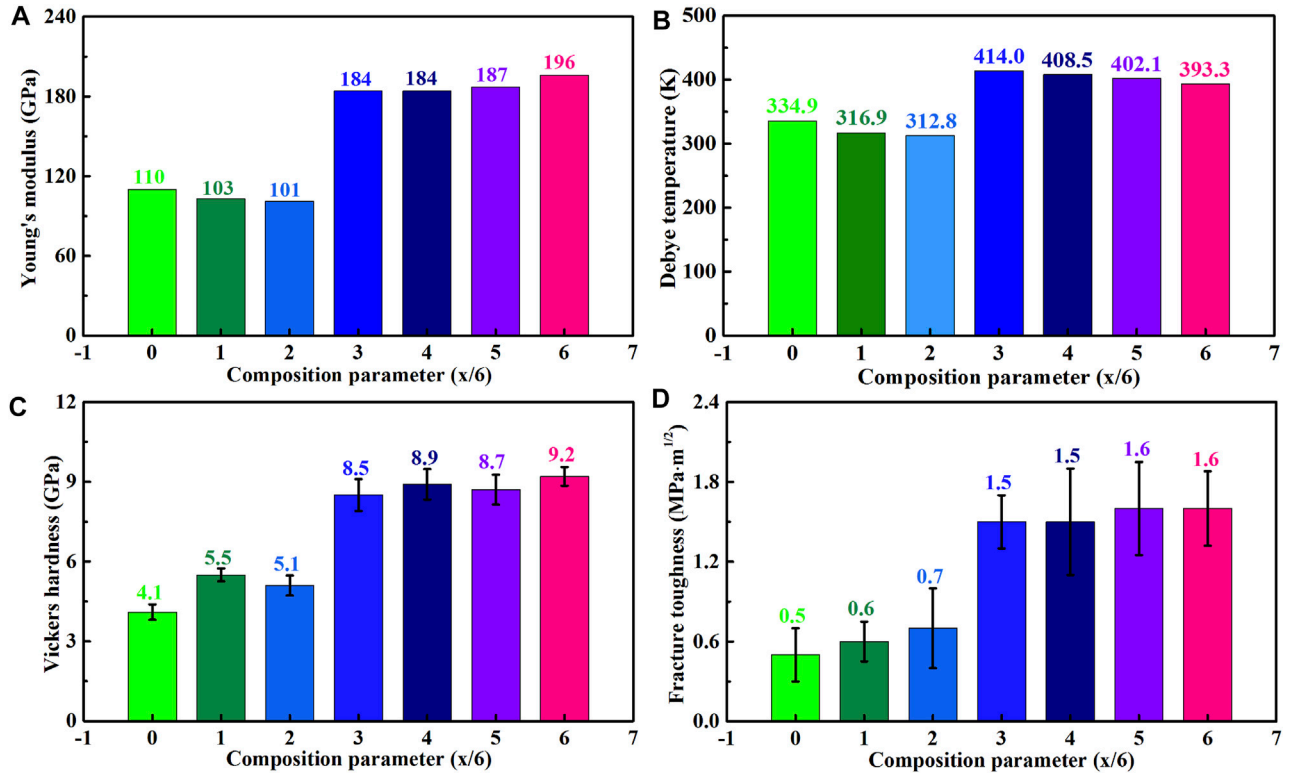

FIGURE 4 | Mechanical properties of $(La_{1-x}Ho_x)_3NbO_7$ (x = 0/6, 1/6, 2/6, 3/6, 4/6, 5/6, and 6/6) ceramics: **(A)** Young's modulus, **(B)** Debye temperature, **(C)** Vickers hardness, and **(D)** fracture toughness.

TABLE 2 | The average acoustic velocity (V_a/m·s^{-1}), Young's modulus (E/GPa), hardness (H/GPa), Debye temperature (Θ_D/K), Poisson's ratio (υ), and fracture toughness (KIC/MPa·m$^{1/2}$) of (La1-xHox)$_3$NbO$_7$ (x = 0/6, 1/6, 2/6, 3/6, 4/6, 5/6, and 6/6) ceramics.

x	*Va*	*E*	*H*	K_{IC}	Θ_D	υ
0/6	2703.8	110.9	4.1 ± 0.29	0.5 ± 0.20	334.9	0.267
1/6	2591.3	103.7	5.5 ± 0.24	0.6 ± 0.16	316.9	0.244
2/6	2544.7	101.8	5.1 ± 0.38	0.7 ± 0.31	312.8	0.283
3/6	3343.1	184.3	8.5 ± 0.60	1.5 ± 0.20	414.0	0.249
4/6	3297.1	184.1	8.9 ± 0.57	1.5 ± 0.40	408.5	0.256
5/6	3221.9	187.0	8.7 ± 0.56	1.6 ± 0.38	402.1	0.263
6/6	3105.4	196.2	9.2 ± 0.35	1.6 ± 0.28	393.3	0.282

$$TSR = \frac{\sigma_f (1 - \upsilon)}{E \cdot TECs}, \tag{4}$$

where σ_f is the flexural strength and υ is Poisson's ratio. Evidently, comparatively low modulus is necessary for maintaining high hardness and good thermal stress fracture resistance, which is essential for the lifetime of TBCs. Besides, the highest fracture toughness of $(La_{1-x}Ho_x)_3NbO_7$ is lower than that of YSZ (3.5 MPa·m$^{1/2}$), but it is better than that of $La_2Zr_2O_7$ (1.0 MPa·m$^{1/2}$) (Schlichting et al., 2001; Yang et al., 2016; Liu et al., 2019).

The variations of aforementioned properties are affected by bonding strengths, which are dominated by the following factors. First, lattice shrinkages caused by the decrements of r_{RE} result in the enhancements of bonding strength as that bonding strengths increase with the decrease of bonding lengths (Zhao et al., 2016; Wang et al., 2018). Second, the Ho–O bonds have higher strengths than La–O bonds, which is reflected by their modulus and Debye temperatures. Third, **Figure 3** shows that the grain size of $(La_{1-x}Ho_x)_3NbO_7$ is decreased by the increased Ho content. The decrements of grain size will lead to increases of grain boundary density, fracture toughness, and hardness.

Thermal Properties

Figures 5A,B,D exhibit that thermal diffusivity and conductivity, and phonon mean free path of $(La_{1-x}Ho_x)_3NbO_7$ solid solutions have the similar temperature dependences because they are dominated by phonons. At room temperature, Ho_3NbO_7 has the lowest thermal diffusivity (0.34 mm^2/s), and conductivity (0.96 W·m^{-1}·K^{-1}) contributed to its disorder cubic fluorite lattice (Chen et al., 2021a; Yang et al., 2019; Chen et al., 2018b). Amorphous thermal conductivity is found in Ho_3NbO_7, when the remaining prepared samples exhibit different temperature dependences of thermal conductivity. The low thermal conductivity originates from the short phonon mean free path shown in **Figure 5D**. The lowest value of k (1.06 W·m^{-1}·K^{-1}) at 900°C is found in $(La_{3/6}Ho_{3/6})_3NbO_7$, and it has the shortest l (0.29 nm). It is evident that $(La_{1-x}Ho_x)_3NbO_7$ has much lower thermal conductivity (0.96–1.42 W·m^{-1}·K^{-1}) than YSZ

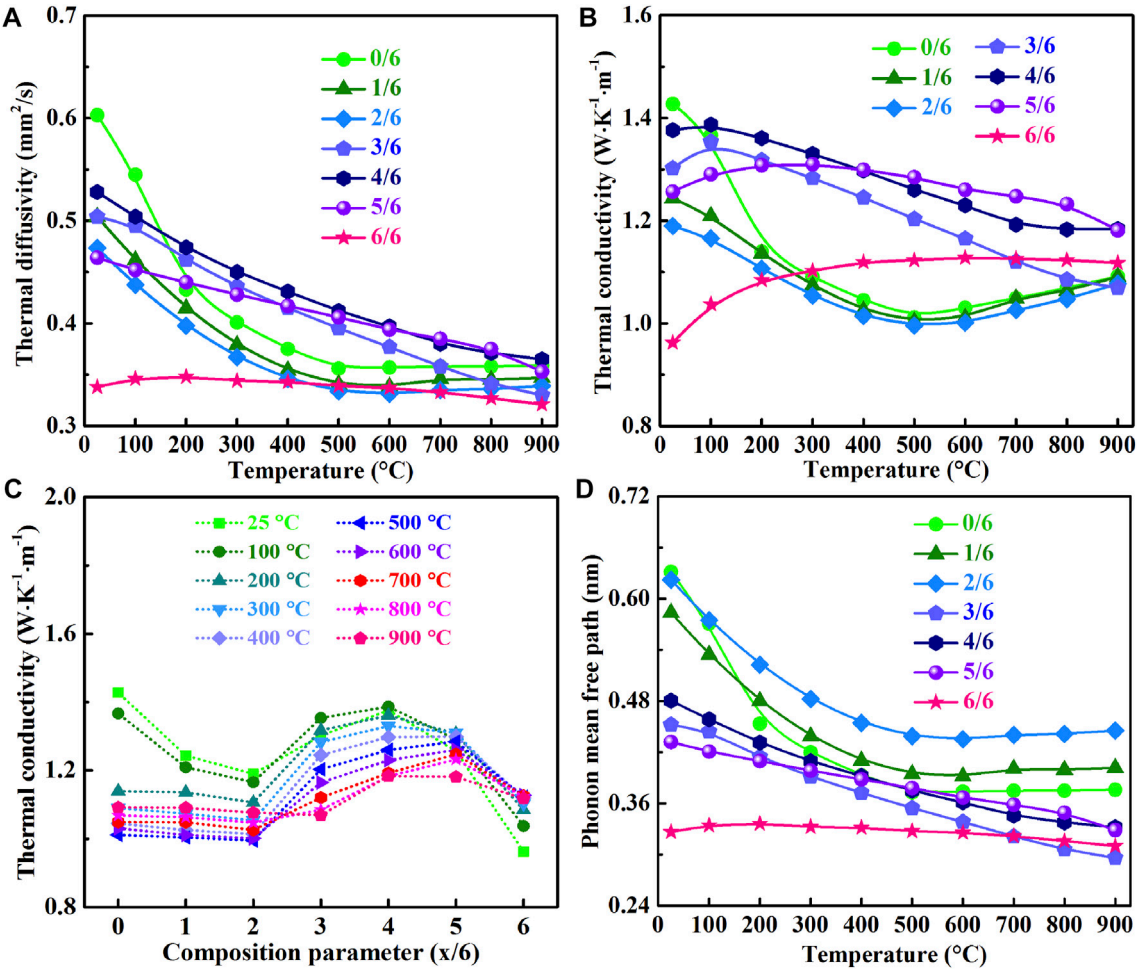

FIGURE 5 | Thermal properties of $(La_{1-x}Ho_x)_3NbO_7$ (x = 0/6, 1/6, 2/6, 3/6, 4/6, 5/6, and 6/6) ceramics: **(A)** thermal diffusivity, **(B)** temperature dependence of thermal conductivity, **(C)** composition dependence of thermal conductivity, and **(D)** phonon mean free path.

(2.50–3.45 $W \cdot m^{-1} \cdot K^{-1}$), $La_2Zr_2O_7$ (1.45–2.58 $W \cdot m^{-1} \cdot K^{-1}$), $LaNbO_4$ (1.43–3.18 $W \cdot m^{-1} \cdot K^{-1}$), and other candidate oxides (Vassen et al., 2000; Feng et al., 2013; Zhao et al., 2016; Chen et al., 2018b; Li et al., 2018; Liu et al., 2019; Ren et al., 2019; Liu et al., 2020a; Liu et al., 2020b; Chen et al., 2020; Ren et al., 2020; Wu et al., 2020; Chen et al., 2021a; Chen et al., 2021b).

During the substitution process of $(La_{1-x}Hox)_3NbO_7$, misfits of atomic mass and ionic size are introduced to the lattice to enhance phonon scattering strength, and thermal conductivity is reduced (Wang et al., 2012; Feng et al., 2013; Zhao et al., 2016; Liu et al., 2019; Liu et al., 2020b). Normally, thermal conductivity decreases with the increasing phonon scattering strength caused by point defects, which can be reflected by the phonon scattering coefficient. It is believed that the phonon scattering coefficient of $(La_{3/6}Ho_{3/6})_3NbO_7$ reaches the maximum based on phonon point defect scattering theory. However, besides phonon point defect scattering, influence of phonon propagation speed on thermal conductivity should be considered according to the evident variations of sound speed. The average acoustic velocities of $(La_{1-x}Ho_x)_3NbO_7$ (x = 3/6, 4/6, 5/6, 6/6) (3,100–3,400 ms^{-1}) are far higher than those of rest samples (2,500–2,700 ms^{-1}), indicating that $(La_{1-x}Ho_x)_3NbO_7$ (x = 3/6, 4/6, 5/6, 6/6) oxides have far higher phonon propagation speed than the others. Therefore, the thermal conductivity of $(La_{1-x}Ho_x)_3NbO_7$ (x = 0/6, 1/6, 2/6) decreases with the increasing Ho content, and it increases with the further increments of Ho content in $(La_{1-x}Ho_x)_3NbO_7$ (x = 3/6, 4/6, 5/6) (**Figure 5C**). Both point defect phonon scattering strength and changes in phonon propagation speed play essential roles on regulations of thermal conductivity of $(La_{1-x}Ho_x)_3NbO_7$ ceramics.

Besides thermal conductivity, high TECs are essential for the service of TBCs. **Figure 6A** displays that the deformation of each sample increases with the increasing temperature, and their slopes are almost constant, which are further proved *via* the first-order differential curves depicted in **Figure 6B**. The phase transition and corresponding temperature can be detected by TMA, which have been proven in our previous research studies on RE_3NbO_7 and $RENbO_4$ ceramics (Chen et al., 2018b; Wu et al., 2020). It is believed that $(La_{1-x}Ho_x)_3NbO_7$ ceramics have a stable lattice up to 1,200°C. The TECs of $(La_{1-x}Ho_x)_3NbO_7$ increase with

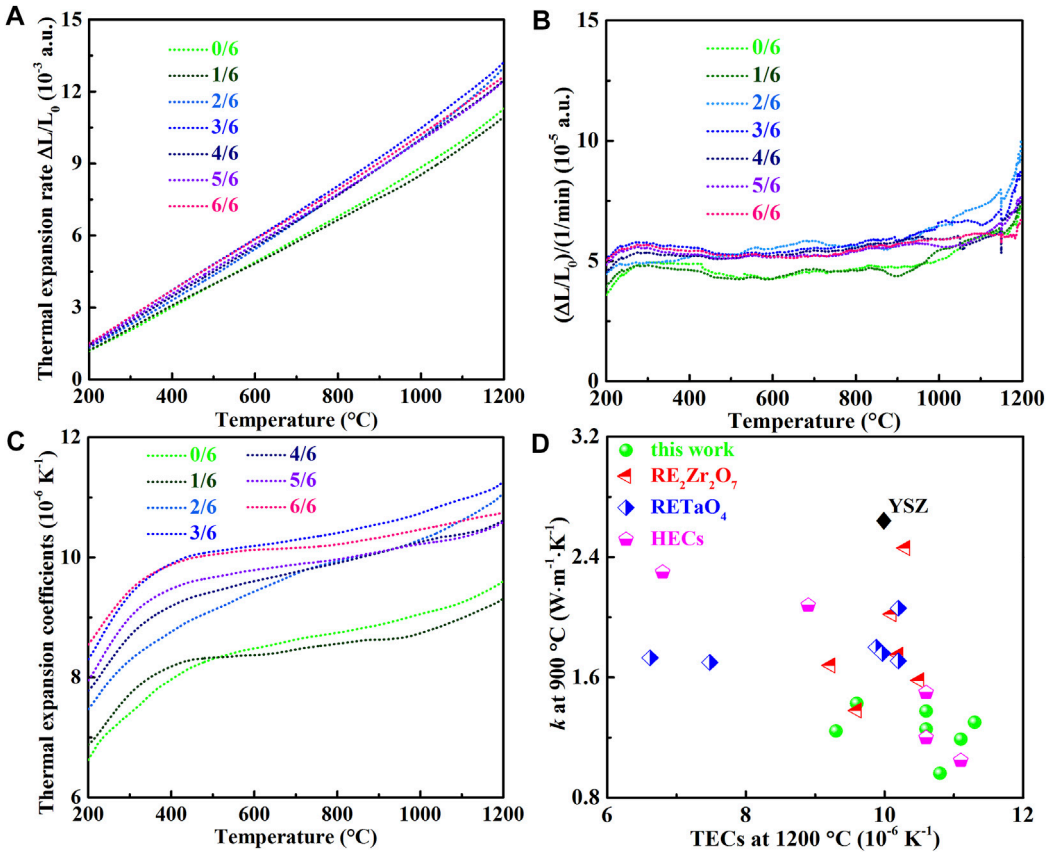

FIGURE 6 | Thermal properties of $(La_{1-x}Ho_x)_3NbO_7$ (x = 0/6, 1/6, 2/6, 3/6, 4/6, 5/6, and 6/6) ceramics: **(A)** thermal expansion rate, **(B)** first-order differential curve, **(C)** thermal expansion coefficients; and **(D)** comparison of thermal conductivity and TECs among various oxide TBCs (Vassen et al., 2000; Schlichting et al., 2001; Zhao et al., 2016; Chen et al., 2018; Ren et al., 2019; Chen et al., 2020; Liu et al., 2020; Liu et al., 2020; Ren et al., 2020; Chen et al., 2021; Chen et al., 2021).

the increments of temperature, as shown in **Figure 6C**, and the maximal value ($11.3 \times 10^{-6}K^{-1}$) at 1,200°C is found in $(La_{3/6}Ho_{3/6})_3NbO_7$. One drawback of YSZ (TECs: $10 \times 10^{-6}\,K^{-1}$) and $RE_2Zr_2O_7$ (TECs: $9 \times 10^{-6}\,K^{-1}$) is the low TECs, which produce high thermal stress during high-temperature applications (Yang et al., 2016; Schlichting et al., 2001; Kingery, 1955; Vassen et al., 2000). The lowest high-temperature thermal conductivity and highest TECs are simultaneously achieved in $(La_{3/6}Ho_{3/6})_3NbO_7$ because of the strongest anharmonic lattice vibrations. Normally, the anharmonic lattice vibrations increase with the increasing temperature, which leads to decrease of thermal conductivity and increase of TECs. The TECs and thermal conductivity of $(La_{1-x}Ho_x)_3NbO_7$ are shown in **Figure 6D** to compare with other TBC oxides. The prepared $(La_{1-x}Ho_x)_3NbO_7$ samples have lower thermal conductivity and higher TECs than current YSZ, $RE_2Zr_2O_7$, $RETaO_4$, and distinct high-entropy ceramics (HECs) (Vassen et al., 2000; Schlichting et al., 2001; Zhao et al., 2016; Chen et al., 2018b; Ren et al., 2019; Liu et al., 2020a; Liu et al., 2020b; Chen et al., 2020; Ren et al., 2020; Chen et al., 2021a; Chen et al., 2021b). It is believed that good thermal insulation performances and low thermal stress can be provided, when $(La_{1-x}Ho_x)_3NbO_7$ ceramics are applied as TBCs.

CONCLUSION

Dense $(La_{1-x}Ho_x)_3NbO_7$ oxide bulks have been fabricated in this work, and their structures and thermophysical properties are characterized. The excellent thermophysical properties indicate that the prepared samples are candidate TBCs, and following conclusions are obtained:

1) Dense and high-purity $(La_{1-x}Ho_x)_3NbO_7$ ceramics are obtained by a solid-state sintering process, and phase transitions of Cmcm→$C222_1$→$Fm\bar{3}m$ *SG* are detected along with the increments of Ho content. The grain sizes are a micron scale, and each element is evenly distributed in these samples.
2) The mechanical properties are affected by their bonding strengths and grain sizes, and the changes of modulus and Debye temperatures prove that their bonding strengths enhance with the increments of Ho content, which is caused by the shortening of bonding length and addition of stiff Ho–O bonds. The highest modulus, hardness, and toughness are 196 GPa, 9.2 GPa, and 1.6 MPa $m^{1/2}$, respectively.

3) Good thermal insulations (k: 1.06 W m^{-1} K^{-1} at 900°C), high TECs (11.3×10^{-6} K^{-1} at 1,200°C), and excellent high-temperature phase stability are simultaneously realized in $(La_{3/6}Ho_{3/6})_3NbO_7$ ceramics, which are far better than those of YSZ, $RE_2Zr_2O_7$, $RETaO_4$, and other TBCs. The intense anharmonic lattice vibrations lead to obvious thermal property improvements.

DATA AVAILABILITY STATEMENT

The original contributions presented in the study are included in the article/Supplementary Material; further inquiries can be directed to the corresponding author.

AUTHOR CONTRIBUTIONS

LC conducted the experiments and wrote this paper, YW and QZ conducted partial experiments on thermal conductivity and thermal expansions, and JF designed the detailed experiments, and discussed and improved this article.

FUNDING

The current work was supported by the National Natural Science Foundation of China (No. 91960103 and 51762028) and Yunnan Province Materials Genome Engineering (No. 2018ZE019).

REFERENCES

Adjaoud, O., and Albe, K. (2021). Nanoindentation of Nanoglasses Tested by Molecular Dynamics Simulations: Influence of Structural Relaxation and Chemical Segregation on the Mechanical Response. *Front. Mater.* 8, 664220. doi:10.3389/fmats.2021.664220

Anderson, O. L. (1963). A Simplified Method for Calculating the Debye Temperature from Elastic Constants. *J. Phys. Chem. Sol.* 24, 909–917. doi:10.1016/0022-3697(63)90067-2

Bruls, R. J., Hintzen, H. T., and Metselaar, R. (2005). A New Estimation Method for the Intrinsic thermal Conductivity of Nonmetallic Compounds. *J. Eur. Ceram. Soc.* 25, 767–779. doi:10.1016/j.jeurceramsoc.2004.05.003

Chen, L., Song, P., and Feng, J. (2018a). Influence of ZrO2 Alloying Effect on the Thermophysical Properties of Fluorite-type Eu3TaO7 Ceramics. *Scripta Materialia*. 152, 117–121. doi:10.1016/j.scriptamat.2018.03.042

Chen, L., Wu, P., Song, P., and Feng, J. (2018b). Potential thermal Barrier Coating Materials: RE 3 NbO 7 (RE =La, Nd, Sm, Eu, Gd, Dy) Ceramics. *J. Am. Ceram. Soc.* 101, 4503–4508. doi:10.1111/jace.15798

Chen, X., Sun, Y., Chen, D., Li, J., Li, W., Zeng, D., et al. (2019a). A Comparative Investigation on the Corrosion Degradation of Plasma Sprayed YSZ and LnMgAl11O19 (Ln = Nd, Sm, Gd) Coatings Exposed to the Molten V2O5 + Na2SO4 Salt Mixture at 1100 °C. *J. Eur. Ceram. Soc.* 39, 3778–3787. doi:10.1016/j.jeurceramsoc.2019.04.055

Chen, L., Hu, M., Wu, P., and Feng, J. (2019b). Thermal Expansion Performance and Intrinsic Lattice thermal Conductivity of Ferroelastic RETaO 4 Ceramics. *J. Am. Ceram. Soc.* 102, 4809–4821. doi:10.1111/jace.16328

Chen, H., Zhao, Z., Xiang, H., Dai, F.-Z., Xu, W., Sun, K., et al. (2020). High Entropy (Y0.2Yb0.2Lu0.2Eu0.2Er0.2)3Al5O12: A Novel High Temperature Stable thermal Barrier Material. *J. Mater. Sci. Technology*. 48, 57–62. doi:10.1016/j.jmst.2020.01.056

Chen, L., Guo, J., Zhu, Y., Hu, M., and Feng, J. (2021a). Features of crystal Structures and Thermo-mechanical Properties of Weberites RE 3 NbO 7 (RE=La, Nd, Sm, Eu, Gd) Ceramics. *J. Am. Ceram. Soc.* 104, 404–412. doi:10.1111/jace.17437

Chen, L., Wang, Y. T., Hu, M. Y., Zhang, L. Y., Wang, J. K., et al. (2021b). Achieved Limit thermal Conductivity and Enhancements of Mechanical Properties in Fluorite RE_3NbO_7 via Entropy Engineering. *Appl. Phys. Lett.* 118, 071905. doi:10.1063/5.0037373

Chen, X., Zhao, Y., Gu, L., Zou, B., Wang, Y., and Cao, X. (2011). Hot Corrosion Behaviour of Plasma Sprayed YSZ/LaMgAl11O19 Composite Coatings in Molten Sulfate-Vanadate Salt. *Corrosion Sci.* 53, 2335–2343. doi:10.1016/j.corsci.2011.03.019

Chen, L., and Feng, J. (2019). Influence of HfO2 Alloying Effect on Microstructure and thermal Conductivity of HoTaO4 Ceramics. *J. Adv. Ceram.* 8, 537–544. doi:10.1007/s40145-019-0336-2

Clarke, D. R. (2003). Materials Selection Guidelines for Low thermal Conductivity thermal Barrier Coatings. *Surf. Coat. Technolog.* 163-164, 67–74. doi:10.1016/s0257-8972(02)00593-5

Feng, J., Xiao, B., Zhou, R., and Pan, W. (2013). Anisotropy in Elasticity and thermal Conductivity of Monazite-type REPO4 (RE=La, Ce, Nd, Sm, Eu and Gd) from First-Principles Calculations. *Acta Materialia*. 61, 7364–7383. doi:10.1016/j.actamat.2013.08.043

Irum, S., Andleeb, S., Sardar, S., Mustafa, Z., Ghaffar, G., Mumtaz, M., et al. (2021). Chemical Synthesis and Antipseudomonal Activity of Al-Doped NiO Nanoparticles. *Front. Mater.* 8, 673458. doi:10.3389/fmats.2021.673458

Kingery, W. D. (1955). Factors Affecting thermal Stress Resistance of Ceramic Materials. *J. Am. Ceram. Soc.* 38, 3–15. doi:10.1111/j.1151-2916.1955.tb14545.x

Kittle, C. (1996). *Introduction to Solid State Physics*. New York: Wiley

Li, Y., Luo, Y., Tian, Z., Wang, J., and Wang, J. (2018). Theoretical Exploration of the Abnormal Trend in Lattice thermal Conductivity for Monosilicates RE2SiO5 (RE = Dy, Ho, Er, Tm, Yb and Lu). *J. Eur. Ceram. Soc.* 38, 3539–3546. doi:10.1016/j.jeurceramsoc.2018.04.014

Liu, B., Liu, Y., Zhu, C., Xiang, H., Chen, H., Sun, L., et al. (2019). Advances on Strategies for Searching for Next Generation thermal Barrier Coating Materials. *J. Mater. Sci. Technology*. 35, 833–851. doi:10.1016/j.jmst.2018.11.016

Liu, M.-J., Zhang, M., Zhang, Q., Yang, G.-J., Li, C.-X., and Li, C.-J. (2018). Gaseous Material Capacity of Open Plasma Jet in Plasma spray-physical Vapor Deposition Process. *Appl. Surf. Sci.* 428, 877–884. doi:10.1016/j.apsusc.2017.09.218

Liu, Y., Jia, D., Zhou, Y., Zhou, Y., Zhao, J., Nian, H., et al. (2020a). Zn0.1Ca0.1Sr0.4Ba0.4ZrO3: A Non-equimolar Multicomponent Perovskite Ceramic with Low thermal Conductivity. *J. Eur. Ceram. Soc.* 40, 6272–6277. doi:10.1016/j.jeurceramsoc.2020.07.054

Liu, Y., Jia, D., Zhou, Y., Zhou, Y., Zhao, J., Li, Q., et al. (2020b). Discovery of ABO4 Scheelites with the Extra Low thermal Conductivity through High-Throughput Calculations. *J. Materiomics* 6, 702–711. doi:10.1016/j.jmat.2020.05.009

Ma, W., Mack, D. E., Vaßen, R., and Stöver, D. (2008). Perovskite-type Strontium Zirconate as a New Material for thermal Barrier Coatings. *J. Am. Ceram. Soc.* 91, 2630–2635. doi:10.1111/j.1551-2916.2008.02472.x

Mielewczyk, G. A., and Navrotsky, A. (2015). Enthalpies of Formation of Rare Earth Niobates, RE_3NbO_7. *Am. Mineral.* 100, 1578–1583. doi:10.2138/am-2015-5210

Padture, N. P., Gell, M., and Jordan, E. H. (2002). Thermal Barrier Coatings for Gas-Turbine Engine Applications. *Science*. 296, 280–284. doi:10.1126/science.1068609

Qu, Z., Wan, C., and Pan, W. (2012). Thermophysical Properties of Rare-Earth Stannates: Effect of Pyrochlore Structure. *Acta Materialia*. 60, 2939–2949. doi:10.1016/j.actamat.2012.01.057

Ren, K., Wang, Q., Shao, G., Zhao, X., and Wang, Y. (2020). Multicomponent High-Entropy Zirconates with Comprehensive Properties for Advanced thermal Barrier Coating. *Scripta Materialia*. 178, 382–386. doi:10.1016/j.scriptamat.2019.12.006

Ren, X., Tian, Z., Zhang, J., and Wang, J. (2019). Equiatomic Quaternary (Y1/4Ho1/4Er1/4Yb1/4)2SiO5 Silicate: A Perspective Multifunctional thermal and Environmental Barrier Coating Material. *Scripta Materialia*. 168, 47–50. doi:10.1016/j.scriptamat.2019.04.018

Schlichting, K. W., Padture, N. P., and Klemens, P. G. (2001). Thermal Conductivity of Dense and Porous Yttria-Stabilized Zirconia. *J. Mater. Sci.* 36, 3003–3010. doi:10.1023/a:1017970924312

Vassen, R., Cao, X. Q., Tietz, F., Basu, D., and Stover, D. (2000). Zirconates as New Materials for thermal Barrier Coatings. *J. Am. Ceram. Soc.* 83, 2023–2028. doi:10.1111/j.1151-2916.2000.tb01506.x

Wang, K., Lan, A. D., and Qiao, J. W. (2021). Corrosion Behavior of $Al_{0.1}$CoCrFeNi High Entropy alloy in Various Chloride-Containing Solutions. *Front. Mater.* 7, 533843. doi:10.3389/fmats.2020.533843

Wang, Y., Xiao, P., Yang, H., Wang, S., Liu, R., and Cao, Y. (2018). Effects of Atom- and Phase-Scale Compressive Stress on Fracture Toughness in Yttrium-Doped Lanthanum Zirconate Solid Solutions. *Ceramics Int.* 44, 6590–6600. doi:10.1016/j.ceramint.2018.01.062

Wang, Y., Yang, F., and Xiao, P. (2012). Glass-like thermal Conductivities in (X = x1 + x2, $0 \leqslant x \leqslant 1.0$) Solid Solutions. *Acta Materialia*. 60, 7024–7033. doi:10.1016/j.actamat.2012.08.063

Wright, A. J., Wang, Q., Huang, C., Nieto, A., Chen, R., and Luo, J. (2020). From High-Entropy Ceramics to Compositionally-Complex Ceramics: a Case Study of Fluorite Oxides. *J. Eur. Ceram. Soc.* 40, 2120–2129. doi:10.1016/j.jeurceramsoc.2020.01.015

Wu, F., Wu, P., Zhou, Y., Chong, X., and Feng, J. (2020). The Thermo-mechanical Properties and Ferroelastic Phase Transition of RENbO 4 (RE = Y, La, Nd, Sm, Gd, Dy, Yb) Ceramics. *J. Am. Ceram. Soc.* 103, 2727–2740. doi:10.1111/jace.16926

Xiang, H., Xing, Y., Dai, F.-z., Wang, H., Su, L., Miao, L., et al. (2021). High-entropy Ceramics: Present Status, Challenges, and a Look Forward. *J. Adv. Ceram.* 10, 385–441. doi:10.1007/s40145-021-0477-y

Yang, J., Qian, X., Pan, W., Yang, R., Li, Z., Han, Y., et al. (2019). Diffused Lattice Vibration and Ultralow thermal Conductivity in the Binary Ln-Nb-O Oxide System. *Adv. Mater.* 31, 1808222. doi:10.1002/adma.201808222

Yang, J., Wan, C., Zhao, M., Shahid, M., and Pan, W. (2016). Effective Blocking of Radiative thermal Conductivity in La2Zr2O7/LaPO4 Composites for High Temperature thermal Insulation Applications. *J. Eur. Ceram. Soc.* 36, 3809–3814. doi:10.1016/j.jeurceramsoc.2016.03.010

Ye, B., Wen, T., Nguyen, M. C., Hao, L., Wang, C.-Z., and Chu, Y. (2019). First-principles Study, Fabrication and Characterization of (Zr0.25Nb0.25Ti0.25V0.25)C High-Entropy Ceramics. *Acta Materialia*. 170, 15–23. doi:10.1016/j.actamat.2019.03.021

Zhang, H. M., Yan, F., Chen, X. G., Zhang, H. S., Liu, Y. X., Tang, A., et al. (2017). Thermal Properties of La_3TaO_7 and La_2AlTaO_7 Oxides. *Ceram. Int.* 43, 755–759. doi:10.1016/j.ceramint.2016.10.005

Zhang, H. S., Feng, Y., Tong, Y. P., Sang, W. W., Zhao, Y. T., Yan, X. F., et al. (2020). Thermal-physical Performances of Novel Pyrochlore-type $Ca_3Ln_3Ce_7Ta_2O_{26.5}$(Ln=Nd and Dy) Oxides. *Ceram. Int.* 46, 11416–11420. doi:10.1016/j.ceramint.2020.01.027

Zhang, H., Sun, J. B., Sun, J., Duo, S., Zhou, X., Yuan, J., et al. (2019). Thermal and Mechanical Properties of Ta2O5 Doped La2Ce2O7 thermal Barrier Coatings Prepared by Atmospheric Plasma Spraying. *J. Eur. Ceram. Soc.* 39, 2379–2388. doi:10.1016/j.jeurceramsoc.2019.02.041

Zhang, H. S., Yu, H. P., Chen, X. G., Zhao, Y. D., Jiao, H. B., Li, G., et al. (2016). Preparation and Thermophysical Properties of Sm_2YbTaO_7 and Sm_2YTaO_7. *Ceram. Int.* 42, 14695–14699.

Zhang, Y.-X., Zhu, Y.-K., Song, D.-S., Feng, J., and Ge, Z.-H. þ(2021). Excellent Thermoelectric Performance Achieved in Bi2Te3/Bi2S3@Bi Nanocomposites. *Chem. Commun.* 57, 2555–2558. doi:10.1039/d1cc00119a

Zhao, M., Ren, X., Yang, J., and Pan, W. (2016). Thermo-mechanical Properties of ThO2-Doped Y2O3 Stabilized ZrO2 for thermal Barrier Coatings. *Ceramics Int.* 42, 501–508. doi:10.1016/j.ceramint.2015.08.137

Zhou, J. H., Jiang, J. N., Deng, L. H., Huang, J. Q., Yuan, J. Y., and Cao, X. Q. (2021). Influence of Bond Coat on thermal Shock Resistance and thermal Ablation Resistance for Polymer Matrix Composites. *Front. Mater.* 8, 672617. doi:10.3389/fmats.2021.672617

Zhou, X., Chen, T., Yuan, J., Deng, Z., Zhang, H., Jiang, J., et al. (2019). Failure of Plasma Sprayed Nano-zirconia-based thermal Barrier Coatings Exposed to Molten CaO-MgO-Al 2 O 3 -SiO 2 Deposits. *J. Am. Ceram. Soc.* 102, 6357–6371. doi:10.1111/jace.16498

Zhou, Y.-X., Zhou, Y., Wu, P., Song, P., Chong, X.-Y., and Feng, J. (2020). Thermal Properties of Y1−xMgxTaO4−x/2 Ceramics via Anion Sublattice Adjustment. *Rare Met.* 39, 545–554. doi:10.1007/s12598-019-01227-0

Zhu, Y.-K., Guo, J., Chen, L., Gu, S.-W., Zhang, Y.-X., Shan, Q., et al. (2021). Simultaneous Enhancement of Thermoelectric Performance and Mechanical Properties in Bi2Te3 via Ru Compositing. *Chem. Eng. J.* 407, 126407. doi:10.1016/j.cej.2020.126407

Conflict of Interest: The authors declare that the research was conducted in the absence of any commercial or financial relationships that could be construed as a potential conflict of interest.

Copyright © 2021 Chen, Wang, Zheng and Feng. This is an open-access article distributed under the terms of the Creative Commons Attribution License (CC BY). The use, distribution or reproduction in other forums is permitted, provided the original author(s) and the copyright owner(s) are credited and that the original publication in this journal is cited, in accordance with accepted academic practice. No use, distribution or reproduction is permitted which does not comply with these terms.